Efficient Time-Domain Image Formation with Precise Topography Accommodation for General Bistatic SAR Configurations

MARC RODRIGUEZ-CASSOLA
PAU PRATS, Member, IEEE
GERHARD KRIEGER, Member, IEEE
ALBERTO MOREIRA, Fellow, IEEE

Due to the lack of an appropriate symmetry in the acquisition geometry, general bistatic synthetic aperture radar (SAR) cannot benefit from the two main properties of low-to-moderate resolution monostatic SAR: azimuth-invariance and topography-insensitivity. The precise accommodation of azimuth-variance and topography is a real challenge for efficent image formation algorithms working in the Fourier domain, but can be quite naturally handled by time-domain approaches. We present an efficient and practical implementation of a generalised bistatic SAR image formation algorithm with an accurate accommodation of these two effects. The algorithm has a common structure with the monostatic fast-factorised backprojection (FFBP), and is therefore based on subaperture processing. The images computed over the different subapertures are displayed in an advantageous elliptical coordinate system capable of incorporating the topographic information of the imaged scene in an analogous manner as topography-dependent monostatic SAR algorithms do. Analytical expressions for the Nyquist requirements using this coordinate system are derived. The overall discussion includes practical implementation hints and a realistic computational burden estimation. The algorithm is tested with both simulated and actual bistatic SAR data. The actual data correspond to the spaceborne-airborne experiment between TerraSAR-X and F-SAR performed in 2007 and to the DLR-ONERA airborne experiment carried out in 2003. The presented approach proves its suitability for the precise SAR focussing of the data acquired in general bistatic configurations.

Manuscript received August 10, 2009; revised January 28, 2010; released for publication May 24, 2011.

IEEE Log No. T-AES/47/4/942913.

Refereeing of this contribution was handled by R. Adve.

Authors' address: German Aerospace Center (DLR), SAR Technology, Meunchnerstr 20, Wessling, 82234, Germany, E-mail: (marc.rodriguez@dlr.de).

I. INTRODUCTION

Bistatic synthetic aperture radar (SAR) surveys lack, in general, the advantageous symmetry most monostatic SAR surveys have. As a consequence, the bistatic SAR image formation task has a complexity which in most cases has only been approximately addressed. In an analogous manner to the progress of monostatic SAR image formation algorithms, improvements in precision and computational efficiency have become available over time. Normal as this evolution might seem, the accessible knowledge in monostatic SAR processing has often been ignored in new developments.

Most popular fast monostatic algorithms rely on the assumptions of linear trajectories, constant height and constant spatial sampling (velocity of the platform divided by pulse repetition frequency) of the system. For a ranging system such as a radar, the previous assumptions impose in the acquisition geometry a circular cylindrical symmetry essential for understanding the existing focussing approaches: targets placed on a given circular cylinder centred on the trajectory of the radar share the same reference range history, shifted proportionally to the along-track position of the target. Two essential properties emanate from this advantageous symmetry: a) azimuth-invariance, and b) insensitivity to topography. The former guarantees that the data can be focussed efficiently in the Fourier-domain, since focussing is achieved by range history correlation. The latter allows a precise computation of range histories with the sole knowledge of target delays, independently on the three-dimensional (3D) position of the target with respect to the radar. The conclusion is that precise efficient focussing can be accomplished independently of the imaged scene.

From the first days of digital SAR processing [1, 2], most of the monostatic image formation algorithms have been based on the previous assumptions, usually showing a well-established trade-off between accuracy and computational efficiency [3–6]. Unfortunately, there is no such thing as linear trajectories, neither for airborne nor for spaceborne systems, only resolutions not high enough so that the deviations from this ideal case can be neglected. Depending on the particular case, the imaging algorithms have been upgraded with intermediate space-variant corrections to account for the realistic nonlinear trajectories, namely motion compensation [7–10] or varying effective velocities [11–13] for airborne and spaceborne systems, respectively. These corrections, initially developed for low-to-moderate resolutions, are insufficient in high-precision applications, such as airborne repeat-pass interferometric or even high-resolution systems. Whereas the azimuth-invariance of monostatic SAR is conserved within moderately large

scenes, the sensitivity to topographic changes is a real issue in monostatic applications requiring high-quality phase information [14–16].

Among bistatic SAR configurations, a straightforward classification depending on their geometric symmetry (and proximity to the ideal monostatic case) can be established.

1) The constant equal velocities, same track and along-track offset case shows exactly the same circular cylindrical symmetry as the monostatic case. This configuration shares the azimuth-invariance and the topography-insensitivity of ideal monostatic SAR.

2) The constant equal velocities and parallel tracks case has elliptical cylindrical symmetry. The configuration is azimuth-invariant (for a flat constant range line) and topography-sensitive, since the bistatic range histories depend on the monostatic transmitter and receiver slant ranges to the targets.

3) Any other bistatic configuration is, in general, azimuth-variant and topography-sensitive.

In other words, even if the approximation of linear trajectories is assumed, bistatic SAR focussing algorithms need take into account the topographic changes of the imaged scene.

The spatial-variance introduced by realistic topography scenarios in the SAR system response might be difficult to accommodate in efficient implementations of Fourier-domain algorithms. Accordingly, most of the bistatic SAR focussing approaches assume a flat scene for exploiting the remaining symmetries of the acquisition [17–47]. All the previous references are based on a sufficiently accurate match of the bistatic range history, at least for a single target. In particular, references [19], [21], [22], [25], [27], [28], [32], [33], [36], [37], [42], [43], [46], [47] address the problem of matching the azimuth-variance of different bistatic acquisitions with different levels of accuracy. Among them, only [25], [47] can be considered precise and suitable for general bistatic configurations. However, [25] is not a focussing approach in itself, but a method to transform a general bistatic survey into a given monostatic, which might pose problems in terms of phase preservation and a significant increase of the computational burden. Topography accommodation, on the other hand, is only discussed or included in [29], [32], [35], [36], [47]. The reference common to the two subsets, [47], shows an implementation of a fast Fourier-domain approach with space-variant wideband phase corrections (i.e., efficiency-reducing) to compensate for the geometrical approximations of the algorithm. In general, the corrections required in bistatic Fourier-domain SAR image formation range from 1D azimuth blocks for azimuth-invariant configurations (i.e., topography) to 2D range-azimuth blocks in the case of general configurations (i.e., topography and azimuth-variance). As a consequence, this space-variant postprocessing reduces the efficiency of the focussing algorithms, increasing its computational burden as performance increases (e.g., resolution, swath).

One natural solution to accommodate the azimuth-variance and topography-sensitivity of bistatic SAR is focussing in the time-domain using the backprojection algorithm (BP) [48, 49]. Among its classical advantages, BP focussing accuracy does not depend on the carrier wavelength, the desired resolution, the scene size or the imaging configuration. Time-domain image formation offers a further advantage particularly useful in the case of bistatic systems: precise accommodation of irregular sampling schemes. However, the real drawback that prevents the generalised use of BP as a standard SAR focussing algorithm is the large computational burden it requires. Consequently, efficient implementations of BP, known as fast backprojection techniques (FBP), have been successfully applied in both monostatic [50–56] and bistatic SAR [57, 58]. FBP techniques applied to monostatic SAR were first presented in two independent developments [50–52]. References [51] and [52] are based on a two-step split of the synthetic aperture. A similar (two-step) approach including the derivation of the Nyquist requirements for the linear track case was presented in [53]. Reference [50], on the other hand, skipped the limitation of the two-step approach and presented a quad-tree based algorithm introducing the idea of splitting the processing into multiple stages. A similar hierarchical approach was used for tomography shortly afterwards. All the developments of monostatic FBP techniques converged to the fast-factorised backprojection (FFBP) algorithm [55], an optimum approach benefiting from the multi-step factorisation working in an efficient geometry in terms of image sampling. Whereas the structure of the bistatic algorithm remains reasonably unchanged when compared with the monostatic approaches, [57] focusses on the ability of bistatic FBP to accomodate the bistatic range history in a precise manner. The authors of [55] mention in [58] to have successfully extended the FFBP algorithm to the one-stationary bistatic configuration. However, the practical implementation of a precise FBP algorithm for realistic general bistatic acquisitions of realistic scenes includes essential details, like the image reference system and the Nyquist sampling requirements, which are for the first time addressed in the following pages.

This paper proposes an image formation algorithm for general bistatic SAR based on the FFBP approach [55]. Section II describes the new algorithm. Special emphasis is put on the reference system on which the images are computed, particularly advantageous for accommodating both the bistatic acquisition geometry and the topographic variations of the scene in an accurate manner. Furthermore, the Nyquist

sampling requirements for the reference image grid are computed and discussed. Section III proves the validity of the algorithm in realistic scenarios with both simulated and real data of two DLR bistatic experiments: the first TerraSAR-X/F-SAR spaceborne-airborne experiment and the DLR-ONERA joint airborne experiment. Section IV concludes the paper with a short summary.

II. BISTATIC FAST-FACTORISED BACKPROJECTION

A. Direct versus Fast Backprojection

SAR image formation using direct backprojection (DBP) [48] is based on a discrete implementation of the BP integral. The image value at range-azimuth time coordinates $(r_0,t_{a,0})$ is computed as follows

$$i(r_0,t_{a,0}) = \int_T dt_a \cdot \exp\left[\mathrm{j}\cdot\frac{2\pi}{\lambda}\cdot r(t_a;\mathrm{P})\right] \cdot d\left(\frac{r(t_a;\mathrm{P})}{\mathrm{c}},t_a\right) \quad (1)$$

where T is the integration time, the integral is computed along the interval $[-T/2,T/2]$, t_a is the azimuth time, λ is the radar wavelength, P is the target to be mapped on image coordinate $(r_0,t_{a,0})$, $r(t_a;\mathrm{P})$ is the bistatic range history of target P, c is the wave propagation speed, and d are the range-compressed data. As it is common in the development of far-field pulsed SAR focussing algorithms, the stop & go approximation is assumed to hold. Should this not be the case (i.e., the length of the pulse is significant compared with the pulse repetition frequency (PRF), a further correction of the instantaneous Doppler effect would be required [59]; as far as this correction is performed accurately enough, the validity of the results presented in the following pages remains unaffected. The advantage of DBP is explicit in (1): the result of the integral is independent of $r(t_a;\mathrm{P})$, provided this range history be computed with sufficient accuracy.[1] Consequently, the precision of the algorithm does not depend on any other kind of geometric assumptions like Fourier-domain algorithms do. DBP is performed entirely in the time-domain and thus particularly suitable for real-time (or) parallelised implementations. Unfortunately, its huge computational load prevents its generalised use as a standard SAR image formation algorithm, making it only the preferred choice for high-demanding applications.

The FBP algorithm overcomes this weakness by dividing the synthetic aperture in subapertures [53], i.e., the integral of (1) is then computed in the following manner

$$\begin{aligned} i(r_0,t_{a,0}) &= \sum_{k=0}^{K-1} i_k(r_0,t_{a,0}) \\ &= \sum_{k=0}^{K-1}\int_{T/K} dt_a \cdot \exp\left[\mathrm{j}\cdot\frac{2\pi}{\lambda}\cdot r(t_a+\Delta t_a[k];\mathrm{P})\right] \\ &\quad \cdot d\left(\frac{r(t_a+\Delta t_a[k];\mathrm{P})}{\mathrm{c}},t_a+\Delta t_a[k]\right) \end{aligned} \quad (2)$$

where k is an integer, the integrals are computed in interval $[-T/2K,T/2K]$, and $\Delta t_a[k] = -(T/2\cdot K)\cdot(K-2\cdot k-1)$. Since the cross-range resolution of the images i_k is roughly K times worse than the full resolution achieved using the whole synthetic aperture, the number of cross-range samples needed for Nyquist sampling the i_k can also be divided by K with respect to i. Thus, the computational load of FBP compared with DBP is also approximately divided by K. This explanation is rather simplistic, since it does not take into account the additional burden involved in computing the contribution of the subimages i_k to the full-resolution image i. This step often requires a two-dimensional interpolation which, if not performed carefully, increases the computational load to about the same amount of DBP. Essentially, FBP achieves the computational speed-up through a clever error-bounded interpolation of the i_k.

Several implementations of FBP algorithms for SAR are available in the literature [50–55] mostly related to applications where the weaknesses of Fourier-domain algorithms vividly arise. Due to the advantages offered by the smart combination of the subimages and the recursive split of the synthetic aperture, we select reference [55] as basis of our further development. This recursive split of subapertures, included in the "divide and conquer" paradigm, shows a clear analogy with the well-known Cooley-Tukey fast Fourier transform (FFT) algorithm, with which the algorithm shares the asymptotic computational speed-up factor. Analogously to the terminology used in [55], we name the implementation of the algorithm for precise image formation of any azimuth-variant bistatic configuration bistatic fast-factorised backprojection and will abbreviate it in the following by BFFBP.

B. Geometric Model

The geometric model of the analysed bistatic configuration only assumes a transmitter and a receiver. No linear, nor parallel, nor constant-speed trajectories are needed to achieve precise focussing. Similarly, it is not necessary to impose a constant PRF during the acquisition. Due to the difficulty of drawing a general intuitive picture, we use Fig. 1 as an illustration of the geometric model. Despite its lack of generality, we have chosen the

[1] Clearly, only the value of the integral for the target placed at $(r_0,t_{a,0})$ is independent of $r(t_a;\mathrm{P})$; depending on the range history of the targets, the form of the SAR impulse response function may change.

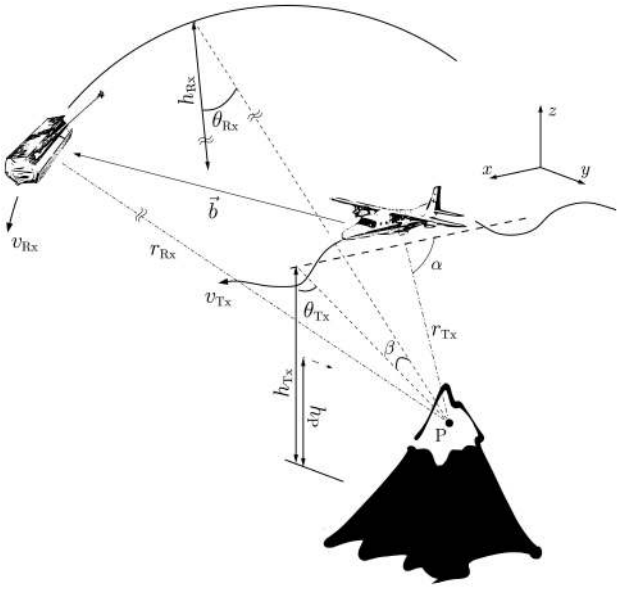

Fig. 1. Bistatic spaceborne-airborne configuration used as illustrative case of general bistatic SAR configuration.

geometry of a spaceborne-airborne bistatic SAR configuration because it encompasses many of the issues only BP algorithms can deal with in a precise manner. Note that the algorithm is able to handle bistatic data of any other configuration (spaceborne-spaceborne, airborne-airborne, one-stationary) up to any desired resolution within the physical constraints of electromagnetic imaging. All available information on the scene topography must be included in the successive focussing stages, due to the three-dimensional dependence of the bistatic range histories. The lack of this information may force to focussing on an image plane, as usually done in conventional moderate-resolution monostatic SAR, but results might not be accurate.

C. Definition of the Subimage Grid

A key point of FBP is an appropriate choice of the grid where the subimages are computed. The subimage grid must be necessarily two-dimensional and sampled near Nyquist. In an analogous manner to typical FBP implementations for the monostatic SAR case, where the subimages are computed on polar grids, we compute our subimages on elliptical grids as the one depicted in Fig. 2. Fig. 2 results from a zenithal view of the configuration shown in Fig. 1. As can be seen in Fig. 1 the depicted vectors and lines are not, in general, on the same plane. Transmitter and receiver, denoted as Tx and Rx, respectively, are placed at the foci of the isorange ellipses. The target P is placed in a three-dimensional space. Without loss of generality, the angular coordinate is defined in Fig. 2 as the angle between the range vector target-transmitter and the transmitter's velocity vector, but might likewise be defined analogously with respect to the receiver. As shown in the upcoming

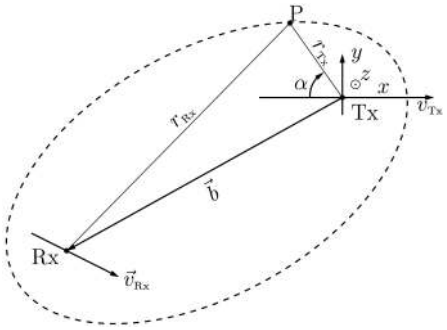

Fig. 2. Reference grid used in BFFBP. P is target whose coordinates in elliptical grid are $(r_{Tx} + r_{Rx}, \alpha)$.

subsection, the preferred choice is the radar with the higher angular velocity, i.e., the rate between the effective velocity and the range to scene. The transformation between the three-dimensional scene into the two-dimensional image grid needs a precise knowledge of the relative position of target P with respect to Tx and Rx. The coordinates of P in the subimage grid are $(r_{Tx} + r_{Rx}, \alpha)$. Comparing this grid with the Cartesian one, the advantage is easily recognisable. Consider the backprojected image of a given scene computed after integration of one single pulse. With respect to the geometry shown in Fig. 2, the x-component of the Cartesian image has a modulation, whereas the elliptical image is constant in the angular dimension, i.e., the cross-range bandwidth of the elliptical image is narrower than that of the Cartesian image. A quantitative and detailed discussion on this essential issue is given in the next subsection. Furthermore, the proposed subimage grid has the advantage of sharing the angular component with the polar grid used in the monostatic case. Thus, it will be sufficient to display the digital elevation model (DEM) in the regular monostatic geometry so that a precise focussing of the bistatic data set is possible.

D. Nyquist Sampling Requirements

Consider two consecutive cross-range samples of the image to be computed and the difference in radar-target range between these two samples. Any range difference higher than the carrier wavelength is not unambiguously retrievable, i.e., is aliased. Along the dimension where the synthetic aperture is built, the Nyquist requirement can be expressed as a function of the wavelength as

$$|\Delta r| \leq \frac{\lambda}{2} \tag{3}$$

where Δr represents the bistatic range difference between consecutive samples. This range difference depends on both the position of the radar and those of the considered samples. In other words, Δr does not remain constant either within an image computed with a given subaperture nor at the same samples of

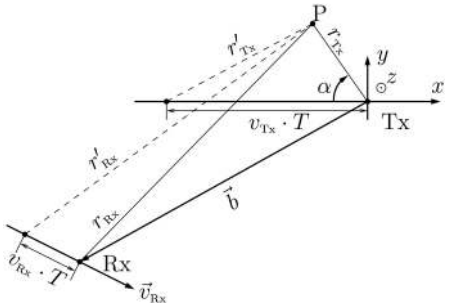

Fig. 3. Computation of bistatic range $r'_{Tx} + r'_{Rx}$ of target $P(r_{Tx} + r_{Rx}, \alpha)$, in relative along-track position $-T$.

images computed with consecutive subapertures, a direct consequence of the azimuth- and spatial-variant character of bistatic acquisitions. Hence, there is no analytical expression matching a unique sampling for all points of a scene and a given subaperture, nor does the sampling requirement remain constant for consecutive subimages. The only precise way of computing the bistatic Nyquist requirements is to do it in a numerical manner. However, under certain assumptions, an operative analytical expression for the Nyquist requirements can be derived. Such an expression can be used (carefully) during processing steps to avoid the need of performing other precise, but slow, numerical computations.

In the derivation of the analytical Nyquist sampling requirements, the following approximations are made: 1) flat Earth geometry, 2) constant speed vectors, and 3) constant heights of the platforms. These approximations, valid in many practical SAR scenarios, will only be used to simplify the trajectories of transmitter and receiver to obtain an operative analytical expression. The processing is naturally done on realistic scenes without any trajectory approximations. For the cases where the previous approximations do not hold, a numerical evaluation of the Nyquist requirements might be necessary, or, as is common in the monostatic case, an appropriate, and usually small, oversampling factor might be used. The three-dimensional scene is defined using a reference system whose origin is placed in the nadir position of the transmitter (cf. Fig. 2). The height of the transmitter over the target P is z_{Tx}. The baseline vector in Cartesian coordinates, denoted as $\vec{b}$, is defined as (b_x, b_y, b_z). Under these assumptions, the Cartesian position of the target P is $(-r_{Tx} \cdot \cos\alpha, \sqrt{r_{Tx}^2 \cdot \sin^2\alpha - z_{Tx}^2}, 0)$. The transmitter and receiver positions at the considered instant are $(0, 0, z_{Tx})$ and $(b_x, b_y, b_z + z_{Tx})$, respectively. Denoting $r = r_{Tx} + r_{Rx}$, and accounting for the looking direction of the acquisition, both monostatic slant ranges r_{Tx}, r_{Rx} can be expressed as a (cumbersome) function of the subimage coordinates (r, α) and the parameteres of the reference grid $\vec{b}$ and z_{Tx}. The transmitter velocity vector is defined as $\vec{v}_{Tx} = (v_{Tx}, 0, 0)$; the receiver velocity vector is defined as $\vec{v}_{Rx} = (v_{Rx,x}, v_{Rx,y}, 0)$, respectively. Without loss of generality, we assume that the scene is placed in halfspace with positive y. We further assume in the following computations that transmitter and receiver contributions to Δr are much smaller than the respective monostatic slant ranges, something common in the SAR case. The monostatic slant ranges to target P at the radar position $-T$ are

$$r'_{Tx}(P) = (r_{Tx}^2 + v_{Tx}^2 \cdot T^2 - 2 \cdot v_{Tx} \cdot T \cdot r_{Tx} \cdot \cos\alpha)^{1/2} \tag{4}$$

$$r'_{Rx}(P) = \Bigg[r_{Rx}^2 + v_{Rx}^2 \cdot T^2 - 2 \cdot T \cdot \Big(v_{Rx,x} \cdot (b_x + r_{Tx} \cdot \cos\alpha) + v_{Rx,y} \cdot \Big(\sqrt{r_{Tx}^2 \cdot \sin^2\alpha - z_{Tx}^2} - b_y \Big) \Big) \Bigg]^{1/2}. \tag{5}$$

The consecutive sample to P is denoted as P_Δ. A 2D projection of the geometry used for the following computations is depicted in Fig. 3.

1) *The Cartesian Case*: Consecutive samples of the Cartesian grid are shifted Δx from P, i.e., $P_\Delta(-r_{Tx} \cdot \cos\alpha \pm \Delta x, \sqrt{r_{Tx}^2 \cdot \sin^2\alpha - z_{Tx}^2}, 0)$. The transmitter and receiver ranges to P_Δ at radar position $-T$ are

$$r'_{Tx}(P_\Delta) = (r_{Tx}^2 + \Delta x^2 \mp 2 \cdot \Delta x \cdot r_{Tx} \cdot \cos\alpha + v_{Tx}^2 \cdot T^2 - 2 \cdot v_{Tx} \cdot T \cdot (r_{Tx} \cdot \cos\alpha \mp \Delta x))^{1/2} \tag{6}$$

$$r'_{Rx}(P_\Delta) = \Bigg(r_{Rx}^2 + \Delta x^2 \mp 2 \cdot \Delta x \cdot (r_{Tx} \cdot \cos\alpha + b_x) + v_{Rx}^2 \cdot T^2 - 2 \cdot T \cdot \Big(v_{Rx,x} \cdot (b_x + r_{Tx} \cdot \cos\alpha \mp \Delta x) + v_{Rx,y} \cdot \Big(\sqrt{r_{Tx}^2 \cdot \sin^2\alpha - z_{Tx}^2} - b_y \Big) \Big) \Bigg)^{1/2}. \tag{7}$$

The range difference can be approximated as

$$\begin{aligned} \Delta r &= r'_{Tx}(P_\Delta) - r'_{Tx}(P) + r'_{Rx}(P_\Delta) - r'_{Rx}(P) \\ &\approx \frac{0.5 \cdot \Delta x^2 \mp \Delta x \cdot (r_{Tx} \cdot \cos\alpha - v_{Tx} \cdot T)}{r'_{Tx}(P)} \\ &\quad + \frac{0.5 \cdot \Delta x^2 \mp \Delta x \cdot (r_{Tx} \cdot \cos\alpha + b_x - v_{Rx,x} \cdot T)}{r'_{Rx}(P)} \\ &= \pm \Delta x \cdot T \cdot \left(\frac{v_{Tx}}{r'_{Tx}(P)} + \frac{v_{Rx,x}}{r'_{Rx}(P)} \right) + \Delta\rho_x(\Delta x; P). \end{aligned} \tag{8}$$

The term $\Delta\rho_x(\Delta x; P)$ increases with Δx. The variation of the first term is unclear, since T decreases for increasing Δx if Nyquist is fulfilled. Note that for

increasing values of T, or longer apertures, $\Delta\rho_x(\Delta x;\mathrm{P})$ becomes negligible and the Nyquist condition derives in the well-known formula for the synthetic resolution [60], i.e.,

$$\delta x \approx \frac{\lambda}{T}\cdot\left(\frac{v_{\mathrm{Tx}}}{r_{0,\mathrm{Tx}}}+\frac{v_{\mathrm{Rx},x}}{r_{0,\mathrm{Rx}}}\right)^{-1} \tag{9}$$

where $r_{0,\mathrm{Tx}}$ and $r_{0,\mathrm{Rx}}$ are the monostatic zero-Doppler ranges for transmitter and receiver, respectively. Since BFFBP is based on a recursive splitting of the synthetic aperture, the subapertures where DBP is performed correspond to very low values of T. For these cases, the range difference between two samples has a percentually low component dependent on T (thus on resolution gain). Computing nonaliased low-resolution subimages on Cartesian grids thus requires a much higher sampling factor than the actual spatial resolution of the subimages and the expected speed-up factor of BFFBP is neutralised.

As a matter of fact, a more precise analysis of the Nyquist requirements in the Cartesian case should include a possible variation in the relative height of P_Δ with respect to P. However, this complicates the analysis (which in the rigorous case should be done numerically anyway). In practical terms, a moderate oversampling factor like in the presence of platform motion errors suffices to avoid aliasing due to topographic variations.

2) *The Elliptical Case*: In the elliptical grid, the consecutive samples are shifted $\Delta\alpha$ from P, hence at coordinates $(r,\alpha\pm\Delta\alpha)$ of the elliptical grid. Due to the effect of topography, the actual position of P_Δ can be described as

$$\left(-r_{\mathrm{Tx},\pm\Delta\alpha}\cdot\cos(\alpha\pm\Delta\alpha),\ \sqrt{r_{\mathrm{Tx},\pm\Delta\alpha}^2\cdot\sin^2(\alpha\pm\Delta\alpha)-z_{\mathrm{Tx},\pm\Delta\alpha}^2},z_{\mathrm{Tx},\pm\Delta\alpha}-z_{\mathrm{Tx}}\right)$$

where $r_{\mathrm{Tx},\pm\Delta\alpha}$ denotes the reference monostatic transmitter slant range of target P_Δ and $z_{\mathrm{Tx},\pm\Delta\alpha}$, the relative transmitter height to target P_Δ. Analogously, $r_{\mathrm{Rx},\pm\Delta\alpha}$ denotes the reference monostatic receiver slant range to the same target. The transmitter and receiver ranges to P_Δ at radar position $-T$ are

$$r'_{\mathrm{Tx}}(\mathrm{P}_\Delta)=(r_{\mathrm{Tx},\pm\Delta\alpha}^2+v_{\mathrm{Tx}}^2\cdot T^2-2\cdot v_{\mathrm{Tx}}\cdot T\cdot r_{\mathrm{Tx},\pm\Delta\alpha}\cdot\cos(\alpha\pm\Delta\alpha))^{1/2} \tag{10}$$

$$r'_{\mathrm{Rx}}(\mathrm{P}_\Delta)=\left[r_{\mathrm{Rx},\pm\Delta\alpha}^2+v_{\mathrm{Rx}}^2\cdot T^2-2\cdot T\cdot\left(v_{\mathrm{Rx},x}\cdot(b_x+r_{\mathrm{Tx},\pm\Delta\alpha}\cdot\cos(\alpha\pm\Delta\alpha))+v_{\mathrm{Rx},y}\cdot\left(\sqrt{r_{\mathrm{Tx},\pm\Delta\alpha}^2\cdot\sin^2(\alpha\pm\Delta\alpha)-z_{\mathrm{Tx},\pm\Delta\alpha}^2}-b_y\right)\right)\right]^{1/2}. \tag{11}$$

For this case, the range difference can be approximated as

$$\begin{aligned}\Delta r\approx{}&\frac{0.5\cdot(r_{\mathrm{Tx},\pm\Delta\alpha}^2-r_{\mathrm{Tx}}^2)}{r'_{\mathrm{Tx}}(\mathrm{P})}+\frac{0.5\cdot(r_{\mathrm{Rx},\pm\Delta\alpha}^2-r_{\mathrm{Rx}}^2)}{r'_{\mathrm{Rx}}(\mathrm{P})}\\&-v_{\mathrm{Tx}}\cdot T\cdot\frac{[r_{\mathrm{Tx},\pm\Delta\alpha}\cdot\cos(\alpha\pm\Delta\alpha)-r_{\mathrm{Tx}}\cdot\cos\alpha]}{r'_{\mathrm{Tx}}(\mathrm{P})}\\&-v_{\mathrm{Rx},x}\cdot T\cdot\frac{[r_{\mathrm{Tx},\pm\Delta\alpha}\cdot\cos(\alpha\pm\Delta\alpha)-r_{\mathrm{Tx}}\cdot\cos\alpha]}{r'_{\mathrm{Rx}}(\mathrm{P})}\\&-\frac{v_{\mathrm{Rx},y}\cdot T}{r'_{\mathrm{Rx}}(\mathrm{P})}\cdot\left[\sqrt{r_{\mathrm{Tx},\pm\Delta\alpha}^2\cdot\sin^2(\alpha\pm\Delta\alpha)-z_{\mathrm{Tx},\pm\Delta\alpha}^2}-\sqrt{r_{\mathrm{Tx}}^2\cdot\sin^2(\alpha)-z_{\mathrm{Tx}}^2}\right].\end{aligned} \tag{12}$$

The first two terms depend entirely on the topography and do not necessarily increase for small subapertures (small T). The last three terms increase linearly with increasing T and encompass the gain in angular resolution obtained by synthesising larger subapertures: the first two account for the transmitter along-track component of the range error; the last one corresponds to the transmitter across-track component of the range error.

Assuming $r_{\mathrm{Tx},\pm\Delta\alpha}\approx r_{\mathrm{Tx}}$, $r_{\mathrm{Rx},\pm\Delta\alpha}\approx r_{\mathrm{Rx}}$, and $z_{\mathrm{Tx},\pm\Delta\alpha}\approx z_{\mathrm{Tx}}$, a similar approximation as the one made in the Cartesian case by setting the height of target P_Δ equal to zero, and changing the sign of (12), Δr can be approximated as follows

$$\Delta r\approx T\cdot r_{\mathrm{Tx}}\cdot\left[\left(\frac{v_{\mathrm{Tx}}}{r'_{\mathrm{Tx}}}+\frac{v_{\mathrm{Rx},x}}{r'_{\mathrm{Rx}}}\right)\cdot\Delta(\cos\alpha)+\frac{v_{\mathrm{Rx},y}}{r'_{\mathrm{Rx}}}\cdot\left(\sqrt{\sin^2\alpha-\frac{z_{\mathrm{Tx}}^2}{r_{\mathrm{Tx}}^2}}-\sqrt{\sin^2(\alpha+\Delta\alpha)-\frac{z_{\mathrm{Tx}}^2}{r_{\mathrm{Tx}}^2}}\right)\right] \tag{13}$$

where $\Delta(\cos\alpha)=\cos(\alpha\pm\Delta\alpha)-\cos\alpha$. The first term in brackets describes the contribution of the transmitter along-track motion components to the synthetic resolution; the second term describes the contribution to the range variation in the direction of the across-track component of the transmitter. A numerical evaluation of (13) to derive the angular Nyquist requirements (cf. (3)) is valid for most bistatic configurations and has a negligible impact in the overall burden of the algorithm.[2] Come to this point, it becomes evident why the angle α should be defined with respect to the radar having the higher angular velocity, since this minimises the contribution to Δr of the term proportional to $v_{\mathrm{Rx},y}$. In cases in which this contribution is small, i.e., the term $v_{\mathrm{Rx},y}\cdot T\cdot r_{\mathrm{Tx}}/r_{\mathrm{Rx}}$ is significantly smaller than the wavelength, a higher

[2]For special configurations where at least one of the radars has a velocity component in the z-coordinate, a further component proportional to $\omega_{\mathrm{x},z}$ needs be added in (10)–(13).

bound to this range error can be expressed as

$$\Delta r \leq T \cdot r_{\mathrm{Tx}} \cdot \left[\left(\frac{v_{\mathrm{Tx}}}{r'_{\mathrm{Tx}}} + \frac{v_{\mathrm{Rx},x}}{r'_{\mathrm{Rx}}} \right) \cdot \Delta(\cos\alpha) + \left| \frac{v_{\mathrm{Rx},y}}{r'_{\mathrm{Rx}}} \right| \right] \tag{14}$$

where from the safe bound for the angular Nyquist requirement can be found

$$\delta(\cos\alpha) \geq \left| \frac{\lambda - |\omega_{\mathrm{Rx},y}| \cdot T \cdot r_{\mathrm{Tx}}}{T \cdot r_{\mathrm{Tx}} \cdot (\omega_{\mathrm{Tx}} + \omega_{\mathrm{Rx},x})} \right| \tag{15}$$

where ω_{Tx} is the transmitter's instantaneous angular velocity, and $\omega_{\mathrm{Rx},x}$ and $\omega_{\mathrm{Rx},y}$ are the x and y components, respectively, of the receiver's intantaneous angular velocity. These instantaneous angular velocities include the azimuth-variant nature of bistatic SAR in (15). We remind that the instantaneous angular velocity reaches its maximum v/r_0 at monostatic zero-Doppler time and decreases to zero for high-squinted monostatic positions. The numerical estimation of these instantaneous angular velocities is easy to implement, but (15) can be again bounded by including the maximum values of the transmitter's and the x component of the receiver's angular velocities. By setting $\omega_{\mathrm{Rx},y} = 0$, we obtain the compact expression of the angular Nyquist requirement of bistatic general along-track acquisitions

$$\delta(\cos\alpha) \geq \frac{\lambda}{T \cdot r_{\mathrm{Tx}} \cdot |\omega_{\mathrm{Tx}} + \omega_{\mathrm{Rx}}|} \tag{16}$$

which reduces to the monostatic expression by setting $\omega_{\mathrm{Rx}} = \omega_{\mathrm{Tx}}$. The influence of the $\omega_{\mathrm{Rx},y}$ is somewhat more complex to quantify, since values of $|\omega_{\mathrm{Rx},y}| \cdot T \cdot r_{\mathrm{Tx}}$ close to the wavelength reduce the information content of (15). Whenever this happens, we need to step back to (13) or even to (12) to derive an estimate of the angular sampling condition.

A second advantage of computing the subimages in elliptical rather than Cartesian grids can be derived even for larger subapertures. Let us assume (9) holds and sampling the Cartesian subimage with this spatial spacing yields no aliasing. Let us assume that the transmitter is placed at the centre of a scene of length L_x, which corresponds to a worst case. Then, the angular length of the scene in $\cos\alpha$ is

$$L_\alpha = \frac{2 \cdot L_x}{\sqrt{L_x^2 + 4 \cdot r_{\mathrm{Tx}}^2}} \tag{17}$$

which yields a necessary number of samples below

$$N_\alpha = \frac{L_\alpha}{\delta(\cos\alpha)} \leq \frac{2 \cdot L_x \cdot T \cdot r_{\mathrm{Tx}} \cdot (\omega_{\mathrm{Tx}} + \omega_{\mathrm{Rx}})}{|\lambda - |\omega_{\mathrm{Rx},y}| \cdot T \cdot r_{\mathrm{Tx}}| \cdot \sqrt{L_x^2 + 4 \cdot r_{\mathrm{Tx}}^2}}. \tag{18}$$

Consequently, we can use (18) matched for the quasi-along-track bistatic configurations ($\omega_{\mathrm{Rx},y} \cdot T \cdot r_{\mathrm{Tx}} \ll \lambda$) to state the further benefit of using elliptical

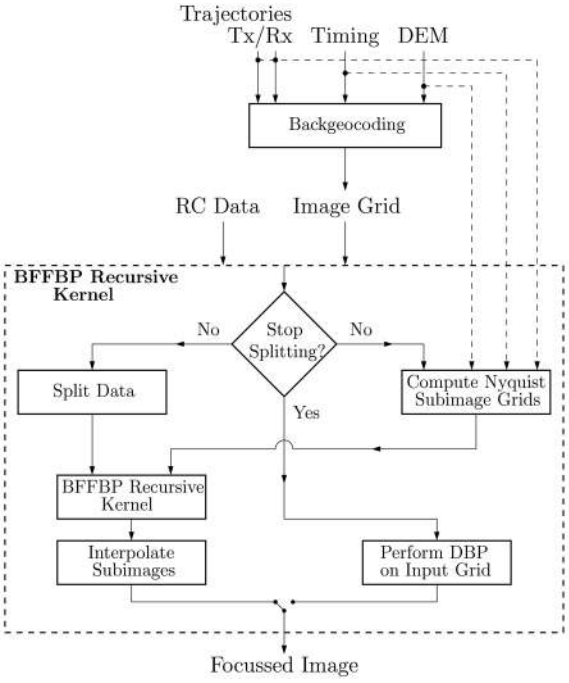

Fig. 4. Block diagram of non-real-time recursive BFFBP implementation. Acronym RC before data stands for range compressed.

grids for backprojecting moderate-to-high resolution subimages. Comparing N_α with the number of samples needed for the Cartesian subimage, noted N_x, we obtain

$$\begin{aligned} N_\alpha &= N_x \cdot \eta \\ &\approx N_x \cdot \frac{\omega_{\mathrm{Tx}} + \omega_{\mathrm{Rx}}}{\max[\omega_{\mathrm{Tx}}] + \max[\omega_{\mathrm{Rx}}]} \cdot \frac{1}{\sqrt{1 + \dfrac{L_x^2}{4 \cdot r_{\mathrm{Tx}}^2}}} \end{aligned} \tag{19}$$

a quite illustrative result, since the factor η is strictly smaller than unity, especially for cases where the length of the scene approaches or even exceeds the slant ranges of the targets. As a result, we conclude that focussing the bistatic subimages on the proposed elliptical grid is a more efficient choice than doing it on the corresponding Cartesian grid. Once all the lower resolution subimages have been computed, the full resolution bistatic image with no aliasing can be interpolated at a last stage into the more convenient visualisation Cartesian grid with small computational cost.

E. Implementation

The block diagram of a non-real-time BFFBP implementation is shown in Fig. 4. The first stage must necessarily be the computation of the scene topography in a convenient coordinate system. A very advantageous solution is a regular monostatic backgeocoding of the imaged scene, since the elliptical grids only contain monostatic angular

information. This backgeocoded DEM is used in the computations of all the subimage grids involved in BFFBP splitting stages, as well as in the computation of the full-resolution Cartesian grid. After this, the algorithm enters its recursive kernel, where a decision must be made whether DBP on the input grid is computed or splitting of the input data continues. Every split of the input data requires a split of the radar trajectories and a computation of new lower resolution elliptical grids. The backgeocoded DEM should however not be decimated if the best topography accommodation (within the resolution of the input DEM) is to be achieved. The computation of DBP on the lowest resolution elliptical grid outputs back to the previous stage of recursion, where all the subimages are interpolated into the higher resolution elliptical grids. This interpolation is the main error source of BFFBP, provided that all Nyquist requirements are fulfilled, and must be carried out carefully. Unfortunately, it is also the computational bottleneck of the algorithm. The good news here is that high-quality interpolators are easy to come by and easily parallelisable. As usual, the quality of the output image is a trade-off between accuracy and computational time. After interpolation of two consecutive higher resolution subimages, the algorithm goes back another stage and repeats. Note that the interpolation of increasing resolution polar grids is one of the highlights of [55], since it minimises the number of required interpolations by always computing subimages on the best possible working grids. We keep this essential feature in our implementation by always using elliptical grids for the subimage computations. Moreover, since all elliptical grids contain the topographic information of the scene up to the required resolution, topography accommodation is naturally achieved in the increasing resolution subimages. If no external DEM is available, processing over a flat scene is also possible but results might not be accurate depending on the bistatic configuration and the required resolutions. The last step of the algorithm includes an interpolation of the highest resolution subimages computed on the finest elliptical grids to the input Cartesian grid (or to any desired projection, e.g., UTM) for better visualisation purposes.

For simplicity, we have only analysed an unweighted spotlight implementation of BFFBP. However, another strong advantage of BP with respect to Fourier-domain techniques is the possibility of precise range- and azimuth-variant antenna filtering and weighting. In addition to the range computations, attitude values of transmitter and receiver for each pulse have to be computed in this case. A two-dimensional weigthing (including notches) has to be generated and assigned only at the lowest resolution stage. Smartly implemented antenna filtering usually reduces the computational burden, since the subimage grids contain less samples. Another strong advantage of FFBP over other Fourier-domain algorithms is the small number of points used in the subapertures. Usually, a slow-time Fourier transform, which can only be performed (unless efficiency-reducing azimuth block-processing is used) once that the data are already recorded, is included in the first stages of any Fourier-domain focussing algorithm. FFBP can start backprojecting low-resolution subimages during the acquisition, during the time any other Fourier-domain algorithm remains idle. Using analogous logic, the memory requirements of the FFBP approach a factor 2 benefit with respect to Fourier-domain techniques, since the data used to backproject low-resolution subimages can readily be discarded before grid interpolation. Last but not least, the effect of working on a pulse-to-pulse basis makes FFBP a good candidate for multithreaded implementations benefitting from the multicore technology used in almost any CPU/GPU produced now.

F. Computational Burden and Memory Consumption

We assume that the backprojected scene has dimensions $N_r \times N_x$ in range and azimuth, respectively. A total of N_a pulses are used in the integration. Since we have assumed spotlight processing, a pulse-to-pulse implementation of bistatic DBP requires a number of operations proportional to

$$N_{\mathrm{DBP}} \propto N_r \cdot N_x \cdot N_a \propto N_r \cdot N_a^2. \tag{20}$$

Considering the linear behaviour of the angular Nyquist requirements presented before (cf. Section IID), and assuming the split factor is 2, subaperture splitting reduces the pure BP effort of the algorithm by a factor 2. Assuming a maximum of K splits of the aperture, the computational burden of the BP part of BFFBP is expressed as

$$N_{\mathrm{BFFBP,\ BP}} = N_{\mathrm{DBP}} \cdot 2^{-K} \tag{21}$$

which, considering $N_a = 2^N$ reduces to

$$N_{\mathrm{BFFBP,\ BP}} \propto N_r \cdot N_a \cdot 2^{N-K}. \tag{22}$$

The computational burden of BFFBP has to be completed by including the grid computations and the grid interpolations. The computation of a grid is proportional to the number of samples of the grid. Let μ_{grid} be the proportionality burden factor of the grid computation; the computational burden of the grids generation throughout the several stages of the algorithm is

$$N_{\mathrm{BFFBP,\ grid}} = \mu_{\mathrm{grid}} \cdot N_r \cdot N_a \cdot K. \tag{23}$$

The interpolation of two grids into a new one is also proportional to the number of samples of the new grid. Analogously to the previous case, let μ_{int} be the proportionality factor of the computational burden of each interpolation, the total computational burden of

the interpolation steps of BFFBP is

$$N_{\text{BFFBP, int}} = 2 \cdot \mu_{\text{int}} \cdot N_r \cdot N_a \cdot K \tag{24}$$

where the factor 2 is caused by the use of two input images to generate one output image in every step of recursion. The speed-up factor of BFFBP with respect to DBP can be expressed as a function of the number of stages K

$$a_{\text{BFFBP}} = \frac{N_{\text{DBP, BP}}}{N_{\text{BFFBP, BP}} + N_{\text{BFFBP, grid}} + N_{\text{BFFBP, int}}} = \frac{2^N}{2^{N-K} + (\mu_{\text{grid}} + 2 \cdot \mu_{\text{int}}) \cdot K}. \tag{25}$$

The factors μ_{grid}, μ_{int} determine the speed-up factor of BFFBP and depend strongly on the implementation. A conservative estimate for the grid computation proportionality factor is $\mu_{\text{grid}} = 1$. The value of μ_{int} depends on the interpolation method used during grid interpolation. A systematic evaluation of the medium- to high-quality interpolation kernels used in FFBP can be found in [61]. As expected, the better the required precision, the slower the grid interpolation and thus the higher the value of μ_{int}, since any interpolated sample is computed using a more or less cumbersome combination of the surrounding samples. If a 2D space-domain interpolator is used, a conservative estimate for the interpolation proportionality factor is $\mu_{\text{int}} = M_r \cdot M_\alpha / 10$, where M_r and M_α are the number of neighbour samples used for the range and angle interpolation, respectively. The advantage of this kind of approache is that the μ_{int} does not increase with increasing image sizes, like is the case if interpolators requiring FFTs are used (e.g., Farrow 2D [62], data upsampling + low-order interpolator). Fig. 5 shows the $\log_2$ of the speed-up factor for a 2D eight-point truncated sinc interpolation kernel (dashed). The value of K coincides with $N - 1$ and so 2-pulse subapertures feed the DBP kernel of BFFBP. For increasing resolutions (increasing N_a), and a constant value of 2^{N-K}, the only factor increasing in the denominator of (25) is K, which is increasing in $\log_2 N_a$. This marks the asymptotic behaviour of the computational speed-up of BFFBP for moderate-to-large apertures. In the figure, the classical speed-up factor of conventional monostatic FBP approaches using lower order interpolators (negligible μ_{grid} and μ_{int}) is also depicted (solid). For small apertures, (25) yields values smaller than unity, and BFFBP spends more time computing and interpolating grids than it takes DBP to compute the full-resolution image. The conclusion is BFFBP does not offer any acceleration for low resolutions when compared with DBP (which is fast anyway), and starts having an edge for moderate and high resolutions, exactly in the same manner Fourier algorithms do. In terms of memory consumption, a pulse-to-pulse implementation of BFFBP retains the advantage of FFBP over DBP of only needing the full-resolution image at the final stage of the processing, allowing for imaginative dynamic memory management strategies.

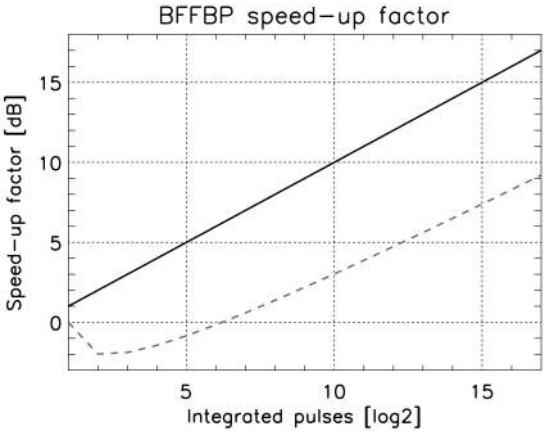

Fig. 5. BFFBP speed-up factor: aymptotic $\log_2$ speed-up factor (solid), eight-point truncated sinc (dashed).

III. EXPERIMENTAL RESULTS

A. Simulated Data: The Old Point Targets

We propose a realistic acquisition over a realistic scene for the simulated data set. We further assume that both transmitter and receiver have exactly the same master frequency and thus perfectly synchronised bistatic data are acquired. A total of four point targets distributed all over Barcelona metropolitan area are generated using the translated motion data of the DLR TerraSAR-X/F-SAR spaceborne-airborne experiment [60]. The height above sea level of F-SAR is lowered to 1167 m to reduce the dimensions of the raw data matrix at the required resolution. Setting the targets in Barcelona has the advantage of having a modest topographic profile which allows to test the ability of the algorithm to accommodate the topographic changes of a realistic scenario. The selected point targets, positions, and heights are listed in Table I. The heights of the considered targets do not include the surrounding buildings. The satellite and the airplane are aligned to reach the centre of the scene at the same instant, though this has no impact on the focussing capabilities of the algorithm. The SAR acquisition parameters are listed in Table II. The range compressed data matrix has dimensions of 8192 samples in range and 32768 samples in azimuth. The expected along-track resolutions for all point targets are modest (significantly better along-track resolutions were measured in [60]), but they are sufficient for the exemplary purpose. The expected resolutions can be found in Table III. The characteristics of the acquisition are demanding, but not pushing the limits. Instead of selecting four-times larger scenes surveyed with a more extreme bistatic configuration with ten-times stronger topographic changes, and intending to achieve resolutions of the order of the wavelength, we choose

TABLE I
Point Targets Position in X-Band Barcelona Simulation

Ref.	Place	Latitude	Longitude	Height
P1.	Mercat de Sant Antoni	45.81239°	43.0027°	12.9 m
P2.	Camp Nou	45.8161°	42.6756°	37.5 m
P3.	Pavelló Mies van der Rohe	45.80449°	42.9029°	36.7 m
P4.	Observatori Fabra	45.85781°	42.6898°	409.8 m

TABLE II
Parameters used in Simulated Data Synthesis

Integration time [s]	3.2768
Pulse repetition frequency [kHz]	10
Ground range scene length [m]	6575
Azimuth scene length [m]	4400
Speed of light [m/s]	$2.9979 \cdot 10^8$
Wavelength [m]	0.031
Transmitted bandwidth [MHz]	300
Sampling frequency [MHz]	330
TerraSAR-X velocity [m/s]	7408
F-SAR velocity [m/s]	90
TerraSAR-X altitude [km]	514
F-SAR altitude [m]	1167

TABLE III
Resolutions of Reference Targets

Target Reference	P1	P2	P3	P4
Along-track resolution [cm]	46.4	53.4	48.9	52.9
Ground-range resolution [cm]	55.3	55.2	55.1	55

the illustrative power of this rather conventional bistatic acquisition over a rather conventional scene of interest in order to compare the obtained results with and without topography accommodation. For this, a realistic DEM of Barcelona is used in the processing steps. The version of BFFBP without topographic accommodation consists of a similar processing using a constant height model of 225 m. BFFBP over this flat grid can be thought of as a higher bound for any Fourier-domain bistatic SAR processing algorithm willing to flee from costly space-variant wide-bandwidth corrections, since precise focussing for the assumed DEM is achieved. The focussed responses with and without topography accommodation are shown in Figs. 6 and 7, respectively. Significant defocussing, even for the ordinary values of the simulation, is found in targets 1 and 3 (located at nearer range) in the case of BFFBP over the flat grid. The four targets appear nicely focussed for the complete version of BFFBP using the DEM information of the scene and their resolution matches the expected values. A 2D truncated sinc interpolator has been used in the implementation of BFFBP used in this section.

B. Real Data: DLR Bistatic SAR Experiments

After the test with simulated data, we proceed to test the algorithm using two bistatic data sets

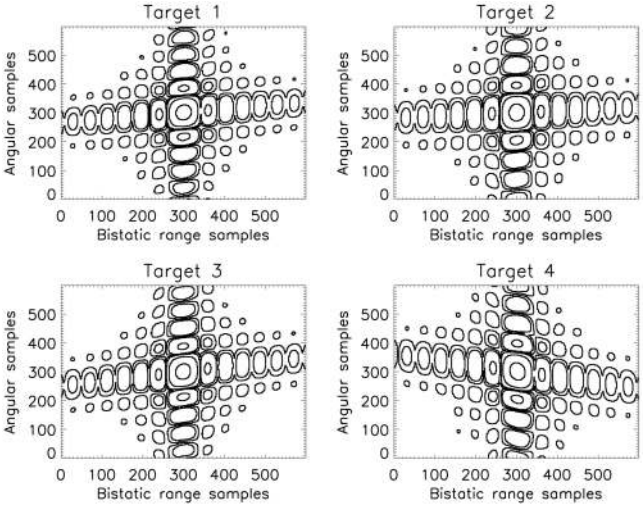

Fig. 6. Simulated point target responses using BFFBP with topography accommodation (realistic external DEM).

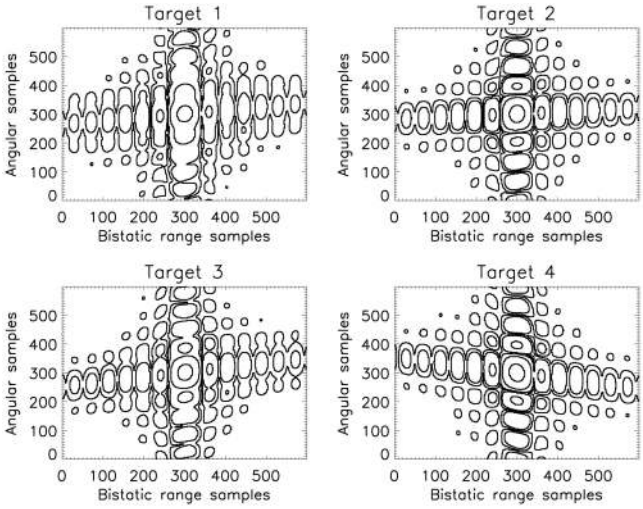

Fig. 7. Simulated point target responses using BFFBP without topography accommodation (flat DEM at 225 m height).

of the DLR bistatic SAR experiments: the first TerraSAR-X/F-SAR spaceborne-airborne experiment, and the DLR-ONERA joint airborne experiment. The first one is used to test the capabilities of a highly azimuth-variant spotlight acquisition, whereas the second one is used to test the algorithm in an azimuth-invariant stripmap acquisition. The effects of the use of two separate master clocks have been previously compensated for before feeding the bistatic data to the BFFBP kernel.

1) *TerraSAR-X/F-SAR Spaceborne-Airborne Experiment*: The data set was acquired during the first TerraSAR-X/F-SAR bistatic spaceborne-airborne experiment, performed in early November 2007 [60]. The experiment was the first one of this kind in Europe, and the first one yielding high-resolution bistatic imaging in a hybrid configuration. The acquisition parameters are listed in Table IV. Further details on image properties and performance

Fig. 8. BFFBP-processed bistatic image of TerraSAR-X/F-SAR first spaceborne-airborne experiment. Radar illumination from top. Bistatic image is shown on full-resolution elliptical grid, which causes slight curvature that can be observed. Low signal parts of image correspond to "nulls" of integrated bistatic azimuth antenna pattern.

of the bistatic system can be found in [60]. The acquisition geometry is a typical bistatic, spotlight and azimuth-variant configuration, with almost parallel tracks, at least in their nadir projections. No modifications with respect to the BFFBP used for the point targets simulation are needed for processing the data. The focussed image is shown in Fig. 8. This image is computed on a full-resolution elliptical grid, as opposed to the usually preferred Cartesian grid for illustration purposes. The use of this elliptical grid can be noticed in the curvature of the airfield runway. The image shows increasing bistatic range from top to

TABLE IV
Acquisition Parameters of TerraSAR-X/F-SAR Experiment

Acquisition mode	Spotlight
Integration time [s]	2.77
Pulse repetition frequency [Hz]	5920
Ground range scene length [m]	7680
Azimuth scene length [m]	2560
Wavelength [m]	0.031
Transmitted bandwidth [MHz]	100
Sampling frequency [MHz]	125
TerraSAR-X effective velocity [m/s]	7408
F-SAR nominal velocity [m/s]	90
TerraSAR-X altitude [km]	514
F-SAR altitude [m]	2180

bottom and increasing angular transmitter information from left to right. No weighting has been introduced in the computation of the BP integral and a wider scene than the dimensions on-ground of the F-SAR antenna pattern has been computed. The integrated F-SAR azimuth antenna pattern can be well observed in the amplitude modulation of the bistatic image, as discussed in [60].

2) *DLR-ONERA Airborne Experiment*: The second data set corresponds to an across-track acquisition of the DLR-ONERA bistatic airborne experiment [63]. Carried out in March 2003, the experiment was the second of its kind in Europe (performed a few days after [64]), and made possible for the very first time the demonstration of cross-platform bistatic SAR interferometry [65, 66]. The bistatic across-track configuration is shown in Fig. 9. The main difference with respect to the previous experiment is the acquisition mode. Whereas the data of the bistatic spaceborne-airborne experiment were acquired in spotlight mode, these are bistatic stripmap data, i.e., antenna filtering is required. The acquisition lasted 96 s, the mean value of the platform velocities was 79.9 m/s and the equivalent Doppler bandwidth synthesised was 200 Hz. Further details on the bistatic configuration can be found in Table V. Fig. 10 shows the focussed bistatic image computed on the full-resolution slant-range/azimuth Cartesian grid. The image shows increasing bistatic range from top to bottom and increasing azimuth from left to right. Again, the contributions to the BP integral have not been weighted. A compensation of the bistatic elevation pattern has been carried out after focussing to improve visualisation. A null of the elevation bistatic pattern can be seen in near range.

3) *Phase Quality Analysis*: To test the usability of BFFBP as a high-precision processor for general bistatic configurations, especially for interferometric applications, we compare the results of Section IIIB1 with an image processed using DBP. For simplicity, we crop the presented image in range and azimuth, and stay within the mainlobe of the illuminated scene, in an area placed between the runway and the

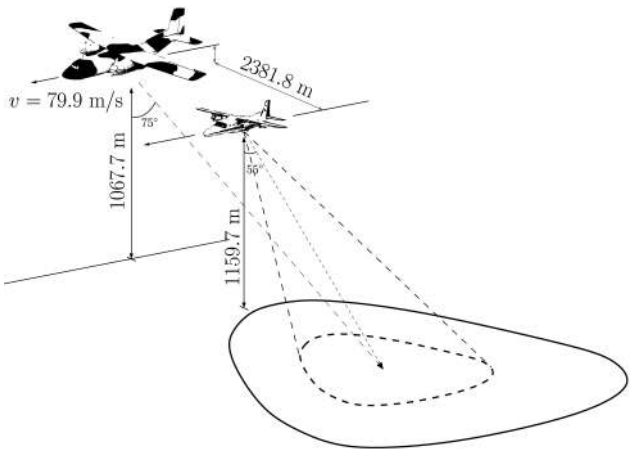

Fig. 9. DLR-ONERA bistatic airborne experiment: across-track configuration.

TABLE V
Acquisition Parameters of DLR-ONERA Bistatic Configuration

Acquisition mode	Stripmap
Doppler bandwidth [Hz]	200
Pulse repetition frequency [Hz]	2000
Slant range scene length [m]	5100
Azimuth scene length [m]	7670
Wavelength [m]	0.03125
Transmitted bandwidth [MHz]	100
Sampling frequency [MHz]	100
RAMSES nominal velocity [m/s]	79.9
E-SAR nominal velocity [m/s]	79.9
RAMSES altitude [m]	1067.7
E-SAR altitude [m]	1159.7
Across-track horizontal baseline [m]	2381.8
Along-track horizontal baseline [m]	127.1

forest. Fig. 11 shows the interferogram of these two images computed over the same elliptical subgrid. A 2D eight-point truncated sinc is used in the image interpolation stages. The mean value of the residual phase error is $-0.013°$ and the standard deviation is $0.89°$.

IV. SUMMARY

The paper has presented the first efficient approach to bistatic SAR image formation capable of precisely accommodating azimuth-variance and topography-dependence, the two main challenging issues when compared with conventional monostatic SAR image formation. The algorithm, based on a subaperture approach, is also well suited for parallelised and real-time implementations, independent of radar wavelength, scene size, or desired resolution. It follows the framework of the monostatic FFBP algorithm, but extends its suitability for general bistatic configurations by presenting an advantageous image coordinate system. The use of the presented elliptical coordinate system allows the display of the topographic information of the scene in monostatic radar coordinates, thus enabling

Fig. 10. BFFBP-processed bistatic image of one across-track configuration of DLR-ONERA airborne experiment. Radar illumination from top. Bistatic image is shown on highest resolution Cartesian grid. Increasing azimuth shown from left to right. Black stripe on top of image corresponds to elevation null of bistatic antenna pattern.

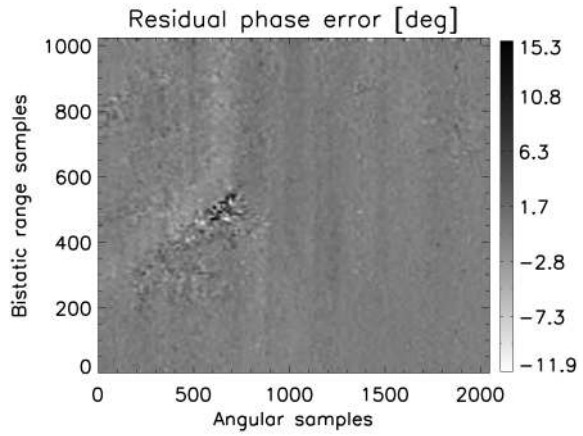

Fig. 11. Residual phase error crop of BFFBP-processed image of first TerraSAR-X/F-SAR bistatic experiment.

topography accommodation in a manner as it is usually carried out in high-precision monostatic SAR processors. The advantage over a more familiar Cartesian coordinate system has been discussed and operative analytical expressions for the Nyquist requirements in the elliptical coordinate system have been derived. The description of the algorithm is complemented with discussions on practical implementation and computational burden. Despite the use of high-quality image interpolators and the need of displaying the scene topography information for every subaperture, the computational speed-up factor of BFFBP is proportional to $\log_2 N$. The algorithm is tested using simulated data representing a realistic bistatic acquisition over Barcelona, where the precise 3D focussing capabilities offered by BFFBP shows a clear advantage over any other 2D processing approach, even for the moderate requirements of the simulation. Bistatic images processed with BFFBP of two different DLR bistatic experiments have also been presented, including phase quality plots using DBP as a valid reference.

ACKNOWLEDGMENTS

We want to thank very warmly Andreas Reigber for his support in the backgeocoding of DEMs and Jesús Selva and Juanma Lopez-Sanchez for their patient and disinterested support on 2D Farrow interpolation.

REFERENCES

[1] Wu, C.
A digital system to produce imagery from SAR.
In *Proceedings of AIAA-SDDS*, Pasadena, CA, 1976.

[2] Cumming, I. G. and Bennett, J. R.
Digital processing of SEASAT SAR data.
In *Proceedings of ICASSP*, 1979, 710–718.

[3] Cafforio, C., Prati, C., and Rocca, F.
SAR data focusing using seismic migration techniques.
IEEE Transactions on Aerospace and Electronic Systems, **27**, 2 (Mar. 1991), 194–207.

[4] Milman, A.
SAR imaging by $\omega - k$ migration.
International Journal of Remote Sensing, **14**, 10 (Mar. 1993), 1965–1979.

[5] Bamler, R.
A comparison of range-Doppler and wavenumber domain SAR focusing algorithms.
IEEE Transactions on Geoscience and Remote Sensing, **30**, 4 (July 1992), 706–713.

[6] Raney, R. K., et al.
Precision SAR processing using chirp scaling.
IEEE Transactions on Geoscience and Remote Sensing, **32**, 4 (July 1994), 786–799.

[7] Moreira, A. and Huang, Y.
Airborne SAR processing of highly squinted data using a chirp scaling approach with integrated motion compensation.
IEEE Transactions on Geoscience and Remote Sensing, **32**, 5 (Sept. 1994), 1029–1040.

[8] Moreira, A., Mittermayer, J., and Scheiber, R.
Extended chirp scaling algorithm for air- and spaceborne SAR data processing in stripmap and ScanSAR imaging modes.
IEEE Transactions on Geoscience and Remote Sensing, **34**, 5 (Sept. 1996), 1123–1136.

[9] Reigber, A., et al.
Extended wavenumber domain SAR focusing with integrated motion compensation.
IEE Proceedings—Radar, Sonar and Navigation, **153**, 3 (June 2006), 301–310.

[10] Cantalloube, H. and Dubois-Fernandez, P.
Airborne X-band SAR imaging with 10 cm resolution: Technical challenge and preliminary results.
IEE Proceedings—Radar, Sonar and Navigation, **153**, 2 (Apr. 2006), 163–176.

[11] Li, F. K., et al.
Doppler parameter estimation for spaceborne synthetic aperture radars.
IEEE Transactions on Geoscience and Remote Sensing, **23**, 1 (Jan. 1985), 47–56.

[12] Cumming, I. G. and Wong, F. H.
Digital Processing of Synthetic Aperture Radar Data. Algorithms and Implementation.
Norwood, MA: Artech House, 2005.

[13] Carrara, W. G., Goodman, R. S., and Majewski, R. M.
Spotlight Synthetic Aperture Radar: Signal Processing Algorithms (IPF).
Norwood, MA: Artech House, 1995.

[14] Prats, P., Reigber, A., and Mallorqui, J. J.
Topography-dependent motion compensation for repeat-pass interferometric SAR systems.
IEEE Geoscience and Remote Sensing Letters, **2**, 2 (Apr. 2005), 206–210.

[15] de Macedo, K. A. C. and Scheiber, R.
Precise topography- and aperture-dependent motion compensation for airborne SAR.
IEEE Geoscience and Remote Sensing Letters, **2**, 2 (Apr. 2005), 172–176.

[16] Prats, P., et al.
Comparison of topography- and aperture dependent motion compensation algorithms for airborne SAR.
IEEE Geoscience and Remote Sensing Letters, **4**, 3 (July 2007), 349–353.

[17] Mensa, D. and Heidbreder, G.
Bistatic synthetic-aperture radar imaging of rotating objects.
IEEE Transactions on Aerospace and Electronic Systems, **AES-18**, 4 (July 1982), 423–431.

[18] Soumekh, M.
Bistatic synthetic aperture radar inversion with application in dynamic object imaging.
IEEE Transactions on Signal Processing, **39**, 9 (Sept. 1991), 2044–2055.

[19] Wong, F. H. and Yeo, T. S.
New applications of non-linear chirp scaling in SAR data processing.
IEEE Transactions on Geoscience and Remote Sensing, **39**, 4 (May 2001), 946–953.

[20] D'Aria, D., Guarnieri, A. M., and Rocca, F.
Focusing bistatic synthetic aperture radar using dip move out.
IEEE Transactions on Geoscience and Remote Sensing, **42**, 6 (July 2004), 1362–1376.

[21] Rigling, B. and Moses, R.
Polar format algorithm for bistatic SAR.
IEEE Transactions on Aerospace and Electronic Systems, **40**, 4 (Oct. 2004), 1147–1159.

[22] Sanz-Marcos, J. and Mallorqui, J. J.
A bistatic SAR simulator and processor.
In *Proceedings of EUSAR*, Ulm, Germany, 2004, 581–584.

[23] Rodriguez-Cassola, M., Krieger, G., and Wendler, M.
Azimuth-invariant, bistatic airborne SAR processing strategies based on monostatic algorithms.
In *Proceedings of IGARSS*, Seoul, South Korea, 2005, 581–584.

[24] Walterscheid, I., et al.
Bistatic SAR processing and experiments.
IEEE Transactions on Geoscience and Remote Sensing, **44**, 10 (Oct. 2006), 2710–2717.

[25] Guarnieri, A. M. and Rocca, F.
Reduction to monostatic focusing of bistatic or motion uncompensated SAR surveys.
IEE Proceedings—Radar, Sonar and Navigation, **153**, 3 (June 2006), 254–310.

[26] Ender, J. G. H., Walterschied, I., and Brenner, A.
Bistatic SAR translational invariant processing and experimental results.
IEE Proceedings—Radar, Sonar and Navigation, **153**, 3 (June 2006), 177–183.

[27] Yates, G., et al.
Bistatic SAR image formation.
IEE Proceedings—Radar, Sonar and Navigation, **153**, 3 (June 2006), 208–213.

[28] Natroshvili, K., et al.
Focusing of general bistatic SAR configuration data with 2-d inverse scaled FFT.
IEEE Transactions on Geoscience and Remote Sensing, **44**, 10 (Oct. 2006), 2718–2727.

[29] Cantalloube, H. and Krieger, G.
Elevation-dependent motion compensation for frequency-domain bistatic SAR image synthesis.
In *Proceedings of IGARSS*, Barcelona, Spain, 2007, 2148–2151.

[30] Bamler, R., Meyer, F., and Liebhart, W.
Processing of bistatic SAR data from quasi-stationary configurations.
IEEE Transactions on Geoscience and Remote Sensing, **45**, 11 (Nov. 2007), 3350–3358.

[31] Zhang, Z.
Focusing parallel bistatic SAR data using the analytic transfer function in the wavenumber domain.
IEEE Transactions on Geoscience and Remote Sensing, **45**, 11 (Nov. 2007), 3633–3645.

[32] Sanz-Marcos, J., et al.
SABRINA: A SAR bistatic receiver for interferometric applications.
IEEE Geoscience and Remote Sensing Letters, **4**, 2 (Apr. 2007), 307–311.

[33] Wong, F. H., Cumming, I. G., and Neo, Y. L.
Focusing bistatic SAR data using the nonlinear chirp scaling algorithm.
IEEE Transactions on Geoscience and Remote Sensing, **46**, 9 (Sept. 2008), 2493–2505.

[34] Neo, Y. L., Wong, F. H., and Cumming, I. G.
Processing of azimuth-invariant bistatic SAR data using the range-Doppler algorithm.
IEEE Transactions on Geoscience and Remote Sensing, **46**, 1 (Jan. 2008), 14–21.

[35] Qiu, X., Hu, D., and Ding, C.
An omega-k algorithm with phase error compensation for bistatic SAR of a translational invariant case.
IEEE Transactions on Geoscience and Remote Sensing, **46**, 8 (Aug. 2008), 2224–2232.

[36] Qiu, X., Hu, D., and Ding, C.
An improved NLCS algorithm with capability analysis for one-stationary BiSAR.
IEEE Transactions on Geoscience and Remote Sensing, **46**, 10 (Oct. 2008), 3179–3186.

[37] Qiu, X., Hu, D., and Ding, C.
Some reflections on bistatic SAR forward-looking configuration.
IEEE Geoscience and Remote Sensing Letters, **5**, 4 (Oct. 2008), 735–739.

[38] Li, F., Li, S., and Zhao, Y.
Focusing azimuth-invariant bistatic SAR data with chirp scaling.
IEEE Geoscience and Remote Sensing Letters, **5**, 3 (July 2008), 484–486.

[39] Li, Y., et al.
Bistatic spotlight SAR processing using the frequency-scaling algorithm.
IEEE Geoscience and Remote Sensing Letters, **5**, 1 (Jan. 2008), 48–52.

[40] Jun, S., Zhang, X., and Yang, J.
Principle and methods on bistatic SAR signal processing via time correlation.
IEEE Transactions on Geoscence and Remote Sensing, **46**, 10 (Oct. 2008), 3163–3178.

[41] Zhong, H. and Liu, X.
An extended nonlinear chirp-scaling algorithm for focusing large baseline azimuth-invariant bistatic SAR data.
IEEE Geoscience and Remote Sensing Letters, **6**, 3 (July 2009), 548–552.

[42] Wang, R., et al.
Focusing spaceborne/airborne hybrid bistatic SAR data uwing wavenumber-domain algorithm.
IEEE Transactions on Geoscence and Remote Sensing, **47**, 7 (July 2009), 2275–2282.

[43] Shin, H. and Lim, J.
Omega-K algorithm for airborne forward-looking bistatic spotlight SAR imaging.
IEEE Geoscience and Remote Sensing Letters, **6**, 2 (Apr. 2009), 312–316.

[44] Liu, B., et al.
Bistatic SAR data focusing using an omega-K algorithm based on method of series reversion.
IEEE Transactions on Geoscence and Remote Sensing, **47**, 8 (Aug. 2009), 2899–2912.

[45] Eldhuset, K.
Spaceborne bistatic SAR processing using the EETF4 algorithm.
IEEE Geoscience and Remote Sensing Letters, **6**, 2 (Apr. 2009), 312–316.

[46] Antoniou, M., Cherniakov, M., and Hu, C.
Space-surface bistatic SAR image formation algorithm.
IEEE Transactions on Geoscence and Remote Sensing, **47**, 6 (June 2009), 1827–1843.

[47] Cantalloube, H.
Non stationary bistatic synthetic aperture radar processing: Assessment of frequency domain processing from simulated and real signals.
In *Proceedings of PIERS*, Beijing, China, 2009, 196–200.

[48] Munson, D. C., O'Brian, J. D., and Jenkins, W. K.
A tomographic formulation of spotlight mode synthetic aperture radar.
Proceedings of the IEEE, **71**, 8 (Aug. 1983), 917–925.

[49] Bauck, J. L. and Jenkins, W. K.
Convolution-backprojection image reconstruction for bistatic synthetic aperture radar.
In *Proceedings of ISCAS*, Portland, OR, July 3–6, 1989, 631–634.

[50] McCorkle, J. and Rofheart, M.
An $N^2 \log_2 N$ backprojector algorithm for focusing wide-angle wide-bandwidth arbitrary-motion synthetic aperture radar.
In *Proceedings of SPIE Aerosense Conference*, Orlando, FL, 1996.

[51] Hellsten, H., et al.
Development of VHF CARABAS II SAR.
In *Proceedings of Radar Sensor Technology, SPIE AeroSense Conference*, Orlando, FL, 1996.

[52] Seger, O., Herberthson, M., and Hellsten, H.
Real-time SAR processsing of low frequency ultra wide band radar data.
In *Proceedings of EUSAR*, vol. 1, Friedrichshafen, Germany, 1998, 489–492.

[53] Yegulalp, A. F.
Fast backprojection algorithm for synthetic aperture radar.
In *Proceedings of the IEEE Radar Conference*, Waltham, MA, Apr. 20–22, 1999, 60–65.

[54] Basu, S. and Y. Bresler, Y.
$O(N^2 \log_2 N)$ filtered backprojection reconstruction algorithm for tomography.
IEEE Transactions on Image Processing, **9**, 10 (Oct. 2000), 1760–1773.

[55] Ulander, L., Hellsten, H., and Stenström, G.
Synthetic aperture radar processing using fast factorized back-projection.
IEEE Transactions on Aerospace and Electronic Systems, **39**, 3 (July 2003), 760–776.

[56] Ulander, L., Frölind, P-O., and Murdin, D.
Fast factorised backprojection algorithm for processing of microwave SAR data.
In *Proceedings of EUSAR*, Dresden, Germany, 2006, 577–580.

[57] Ding, Y. and Munson, Jr., D. C.
A fast back-projection algorithm for bistatic SAR imaging.
In *Proceedings of ICIP*, Pasadena, CA, 2002, 449–452.

[58] Ulander, L., et al.
Bistatic experiment with ultra-wideband VHF synthetic aperture radar.
In *Proceedings of EUSAR*, Friedrichshafen, Germany, 2008, 1–4.

[59] Meta, A., Hoogeboom, P., and Ligthart, L. P.
Signal processing in FMCW SAR.
IEEE Transactions on Geoscience and Remote Sensing, **45**, 11 (Nov. 2007), 3519–3532.

[60] Rodriguez-Cassola, M., et al.
Bistatic TerraSAR-X/F-SAR spaceborne-airborne SAR experiment: Description, data processing and results.
IEEE Transactions on Geoscience and Remote Sensing, **48**, 2 (Feb. 2010), 781–794.

[61] Frölind, P-O. and Ulander, L.
Evaluation of angular interpolation kernels in fast back-projection SAR processing.
IEE Proceedings—Radar, Sonar and Navigation, **153**, 3 (June 2006), 243–249.

[62] Selva, J. and Lopez-Sanchez, J. M.
Efficient interpolation of SAR images for coregistration in SAR interferometry.
IEEE Geoscience and Remote Sensing Letters, **4**, 3 (July 2007), 411–415.

[63] Dubois-Fernandez, P., et al.
ONERA-DLR bistatic SAR campaign: Planning, data acquisition, and first analysis of bistatic scattering behavior of natural and urban targets.
IEE Proceedings—Radar, Sonar and Navigation, **153**, 3 (June 2006), 214–223.

[64] Yates, G., et al.
Bistatic SAR image formation.
In *Proceedings of EUSAR*, Ulm, Germany, Nov. 2004, 208–213.

[65] Cantalloube, H., et al.
Challenges in SAR processing for airborne bistatic acquisitions.
In *Proceedings of EUSAR*, Dresden, Germany, May 2006.

[66] Cantalloube, H., et al.
Bistatic moving target indication using across-track and along-track interferometry.
In *Proceedings of EUSAR*, Dresden, Germany, May 2006.

Marc Rodriguez-Cassola was born in Barcelona, Spain, in 1977. He received the Ingeniero degree in telecommunication engineering from Universidad Pública de Navarra, Pamplona, Spain, in 2000.

From 2000 to 2001, he was a radar hardware engineer at CETP/CNRS, Saint Maur des Fossés, France. From 2001 to 2003, he worked as a software engineer at Altran Consulting in Germany. Since 2003, he has been with the Microwaves and Radar Institute, German Aerospace Center (DLR), Germany, where he has been working on airborne and spaceborne bistatic SAR system analysis and data processing. His current research interests encompass radar signal processing, innovative high-precision SAR imaging algorithms, and bistatic radar system analysis and applications.

Pau Prats (S'03—M'06) was born in Madrid, Spain, in 1977. He received the M.S. degree in telecommunication engineering and the Ph.D. degree from the Universitat Politècnica de Catalunya (UPC), Barcelona, Spain, in 2001 and 2006, respectively.

In 2001, he was with the Institute of Geomatics, Spain, as a research assistant, where he designed a subaperture synthetic aperture radar (SAR) processor. In 2002, he was with the Department of Signal Theory and Communications, UPC, where he worked in the field of airborne repeat-pass interferometry and airborne differential SAR interferometry. From December 2002 to August 2006, he was an assistant professor with the Department of Telecommunications and Systems Engineering, Universitat Autònoma de Barcelona, Barcelona. In 2006, he joined the Microwaves and Radar Institute, German Aerospace Center (DLR), Wessling, Germany, where, since August 2009, he is head of the Multimodal Algorithms Group. His research interests include air- and spaceborne SAR processing, SAR interferometry, differential SAR interferometry and motion compensation for airborne systems.

Dr. Prats was the recipient of the First Prize of the Student Paper Competition of the IEEE International Geoscience and Remote Sensing Symposium 2005 Conference held in Seoul, Korea.

Gerhard Krieger received the Dipl.-Ing. (M.S.) and Dr.-Ing. (Ph.D.) degrees (with honors) in electrical and communication engineering from the Technical University of Munich, Germany, in 1992 and 1999, respectively.

From 1992 to 1999, he was with the Ludwig-Maximilians University, Munich, where he conducted multidisciplinary research on neuronal modeling and nonlinear information processing in biological and technical vision systems. In 1999, he joined the Microwaves and Radar Institute (HR) of the German Aerospace Center (DLR), Oberpfaffenhofen, Germany, where he developed signal and image processing algorithms for a novel forward looking radar system employing digital beamforming on receive. From 2001 to 2007 he led the New SAR Missions Group which pioneered the development of advanced bistatic and multistatic radar systems as exemplified by the forthcoming TanDEM-X mission as well as innovative multi-channel SAR techniques and algorithms for high-resolution wide-swath SAR imaging. Since 2008, he has been Head of the new Radar Concepts Department of the Microwaves and Radar Institute, DLR, Oberpfaffenhofen, Germany.

Dr. Krieger received several national and international awards, including the IEEE Transactions Prize Paper Award of the Geoscience and Remote Sensing Society and the Otto Lilienthal Sabbatical of the German Aerospace Center, DLR. He is author of 30 peer reviewed journal papers, 4 invited book chapters, more than 100 conference papers, and 4 patents. His current research interests focus on the development of multi-channel radar techniques and algorithms for innovative MIMO SAR systems, the demonstration of novel interferometric and tomographic Earth observation applications, and the conceptual design of advanced bi- and multistatic radar missions.

Alberto Moreira (M'92—SM'96—F'04) was born in São José dos Campos, Brazil, in 1962. He received the B.S.E.E. and the M.S.E.E. degrees, in 1984 and 1986, respectively, from the Aeronautical Technological Institute ITA, Brazil and the Eng. Dr. degree (Honors) from the Technical University of Munich, Germany, 1993.

In 2003, he received a full professorship from the University of Karlsruhe, Germany, in the field of microwave remote sensing. As its chief scientist and engineer, he managed from 1996 to 2001 the SAR Technology Department of the Microwaves and Radar Institute at the German Aerospace Center (DLR). Under his leadership, the DLR airborne SAR system, E-SAR, has been upgraded to operate in innovative imaging modes like polarimetric SAR interferometry and SAR tomography. Since 2001, he is the director of the Microwaves and Radar Institute at DLR. The Institute contributes to several scientific programs and space projects for actual and future air- and space-borne SAR missions like TerraSAR-X and Sentinel-1. In 2006, the mission proposal TanDEM-X lead by his Institute has been approved for the realization phase. He is the principal investigator for this mission.

He is serving as a Member of the IEEE GRS-S Administrative Committee (1999–2001, 2004–2007, 2008–2009 as Executive Vice-President), was the founder and chair of the German Chapter of the GRS-S (2003–2008), was an associate editor for the *Geoscience and Remote Sensing Letters* (2003–2007) and is serving since 2005 as associate and guest editor for the *Transactions on Geoscience and Remote Sensing* (TGRS). From 2003 until 2008 he served as a Member of the Board of Directors of the ITG (Information Technology Society) of VDE (German Association for Electrical, Electronic and Information Technologies). In 1995, he was the recipient of the DLR Science Award. He and his colleagues received the GRS-S Transactions Prize Paper Awards in 1997, 2001 and 2007. He is also the recipient of the IEEE Nathanson Award for the Young Radar Engineer of the Year (1999) and the IEEE Kiyo Tomiyasu Field Award (2007). He has contributed to the successful series of the European SAR conferences (EUSAR) since 1996 as Member of the Technical Program Committee, technical chairman (2000), awards chairman (2002–2004), general chairman (2006) and cochairman (2008). He has participated in 19 IGARSS conferences, has more than 250 publications in international conferences and journals and holds 15 patents in the radar and antenna field.

Professor Moreira's professional interests and research areas encompass radar end-to-end system design and analysis, innovative microwave techniques and system concepts, signal processing and remote sensing applications.